

Energy balance for 6D kinetic ions with adiabatic electrons

M. Raeth* and K. Hallatschek

Max Planck Institute for Plasma Physics, Boltzmannstr. 2, 85748 Garching, Germany

(Dated: November 20, 2024)

This paper investigates the energy fluxes for the 6D kinetic Vlasov system. We introduce a novel method for calculating particle and energy flows within this framework which allows for the determination of energy and particle fluxes, as well as the Poynting flux, directly from the system's moments such as kinetic energy density, momentum transfer tensor. The fluxes computed using the new method exhibit fewer gyrooscillations. This approach also enables the identification of both the gyrokinetic $\mathbf{E} \times \mathbf{B}$ heat flux and additional non-gyrokinetic contributions, while simultaneously reducing inherent gyrooscillations in the energy and particle fluxes. Our semi-Lagrangian solver for the 6D kinetic Vlasov system, features a highly efficient scheme to address the $\mathbf{v} \times \mathbf{B}$ acceleration from the strong background magnetic field allows for the simulation of plasma waves and turbulence with frequencies extending beyond the cyclotron frequency, independent of gradient strength or fluctuation levels. The solver has been rigorously tested in the low-frequency regime for dispersion relations and energy fluxes in both linear and nonlinear scenarios.

I. Introduction

Kinetic models can describe phenomena within a tokamak plasma across different scales however, until recently, we lacked the computational capacity for the fully kinetic simulations. Gyrokinetic models used in codes like CGYRO [1], GENE [3] and ORB5 [4], agree well with experiments in fusion device cores but face challenges in high-gradient regimes like the tokamak plasma edge. Most models rely on a δf approximations and break down in these regions of steep gradients and high fluctuation amplitudes. In recent years, there is a growing interest in the instability of ion Bernstein waves (IBWs) [5, 8, 11], including the excitation of turbulent IBWs in steep gradient regions such as the plasma edge [6]. To evaluate the importance of these modes it is important to understand the energy fluxes in the system.

This work provides a comprehensive analysis of the kinetic and electric energy balance for 6D kinetic ions coupled with adiabatic electrons. We introduce a novel method for computing the energy transport which reduces the amount of Larmor oscillations and clearly shows the contributions of different moments of the distribution function to the energy flux, including the $\mathbf{E} \times \mathbf{B}$ energy flux familiar from gyrokinetics, thus establishing a direct connection between the two models. In addition to the analytical description, we compare the new method with the straight-forward summation of the energy fluxes for ITG turbulence simulated with the 6D kinetic Vlasov code BSL6D [9, 10].

After a brief introduction to the physical system in section II, we describe the various energy transport channels, beginning with the energy flux in adiabatic electrons and the Poynting flux (section III), followed by a detailed description of particle and energy transport for kinetic ions. Section V presents simulation results that compare the newly derived energy fluxes with the straight-forward summation.

II. Physical system

The Vlasov equation describes the motion of a plasma in presence of electromagnetic fields. We consider ions in a constant and homogeneous magnetic field $\mathbf{B}_0 = \hat{z}$ represented by a 6D distribution function f , with an electric field \mathbf{E} originating from the interaction with adiabatic electrons. The target of our 6D simulations is the collisionless ion kinetic equation in dimensionless variables ($\rho_i = v_{th} = n_0 = T = 1$, with the ion Larmor radius $\rho_i = \sqrt{m_i T} / (eB)$, the ion thermal velocity $v_{th} = \sqrt{T/m_i}$, the ion background density n_0 and the ion background temperature T)

$$\partial_t f + \mathbf{v} \cdot \nabla f + (-\nabla \phi + \mathbf{v} \times \hat{z}) \cdot \nabla_v f = 0. \quad (1)$$

For simplicity, we assume that the electrons are adiabatic $f_e = e^\phi f_M \approx (1 + \phi) f_M$ [assuming a Maxwellian background distribution $f_M = \exp(-v^2/2) / (2\pi^{3/2})$] and the plasma is quasineutral $n_e = n$ (with the electron density n_e), the electrostatic field is given by

$$\phi = n - 1, \quad n = \int f d^3v. \quad (2)$$

III. Energy balance

1. Electron energy balance

Before computing the energy fluxes of the kinetic ions, we are focusing on the contribution to the energy balance by the electrons. In the following, electron quantities carry an index 'e' (f_e, n_e, T_e , etc.), while quantities without index (f, n, T , etc.) refer to the ions.

For the entire derivation, we consider the quasineutral limit ($\epsilon_0 \rightarrow 0$), the energy contained in the electric field $\epsilon_E = \epsilon_0 E^2/2$ and the Coulomb term $\epsilon_0 \Delta \phi$ are zero. The change of the electron energy density $\partial_t \epsilon_e$ is sum of the divergence of the energy density flux \mathbf{Q}_e and the work performed on the electrons by the electric field $\mathbf{E} \cdot \mathbf{\Gamma}_e$

$$\partial_t \epsilon_e = -\nabla \cdot \mathbf{Q}_e - \mathbf{E} \cdot \mathbf{\Gamma}_e. \quad (3)$$

*Electronic address: Mario.Raeth@ipp.mpg.de

When inserting $\nabla\phi = -\mathbf{E}$ in the last term of (3), it can be rewritten as

$$-\mathbf{E} \cdot \mathbf{\Gamma}_e = (\nabla\phi) \cdot \mathbf{\Gamma}_e = \nabla \cdot (\phi\mathbf{\Gamma}_e) - \phi\nabla \cdot \mathbf{\Gamma}_e, \quad (4)$$

which can be further modified using the continuity equation

$$\partial_t n = -\nabla \cdot \mathbf{\Gamma}_e \quad (5)$$

resulting in

$$-\mathbf{E} \cdot \mathbf{\Gamma}_e = \nabla \cdot (\phi\mathbf{\Gamma}_e) + \phi\partial_t n_e. \quad (6)$$

With quasineutrality equation for adiabatic electrons $\phi = n_e - 1 = n - 1$ (assuming $T_e = 1$) results in

$$\partial_t \frac{(n-1)^2}{2} = -\nabla \cdot (\phi\mathbf{\Gamma}_e) - \mathbf{E} \cdot \mathbf{\Gamma}_e \quad (7)$$

By comparing equations (3) and (7), we can identify expressions for the energy electron density [2]

$$\epsilon_e = \frac{(n-1)^2}{2}, \quad (8)$$

and subsequently, the energy flux density is given by

$$\mathbf{Q}_e = \phi\mathbf{\Gamma}_e. \quad (9)$$

(The adiabatic electrons can be interpreted as local capacitors, since $\phi \propto \delta n$, but for consistency with the Poynting flux, we need to account for the electron currents). (9)

2. Poynting flux

In addition to the energy flux in the electrons, the Poynting flux $\mathbf{S} = \mathbf{E} \times \mathbf{B}/\mu_0$ has to be considered. We rewrite the Poynting flux using $\mathbf{B} = \hat{z} + \delta\mathbf{B}$ and $\mathbf{E} = -\nabla\phi + \partial_t\mathbf{A}$, as

$$\begin{aligned} \mathbf{S} &= \frac{1}{\mu_0} \mathbf{E} \times \mathbf{B} \\ &= \frac{1}{\mu_0} (-\nabla\phi \times \mathbf{B} + \partial_t\mathbf{A} \times \mathbf{B}) \\ &= \underbrace{-\frac{1}{\mu_0} \nabla \times (\phi\mathbf{B})}_{O(\frac{1}{\mu_0})} + \underbrace{\phi \frac{\nabla \times \mathbf{B}}{\mu_0}}_{O(1)} + \underbrace{\frac{\partial_t\mathbf{A}}{\mu_0} \times \hat{z}}_{O(1)} + \underbrace{\frac{\partial_t\mathbf{A} \times \delta\mathbf{B}}{\mu_0}}_{O(\mu_0)}. \end{aligned} \quad (10)$$

Since $\Delta\mathbf{A} = \mu_0\mathbf{j}$ and $\nabla \times \mathbf{B} = \mu_0\mathbf{j}$, we know that $\delta\mathbf{B} = O(\mu_0)$ and $\mathbf{A} = O(\mu_0)$ and thus, $\partial_t\mathbf{A} \times \delta\mathbf{B}/\mu_0 = O(\mu_0)$. In the electrostatic limit, $\mu_0 \rightarrow 0$, most terms of (10) vanish. However, the first term $\nabla \times (\phi\hat{z})/\mu_0 \rightarrow \infty$ because the background magnetic field is externally imposed rather than generated by plasma currents. Since the resulting term is divergence free, it does not contribute to the energy transport and can be ignored in the following discussion of turbulent transport balance. Using Ampère's law, where the displacement current vanishes because of the quasineutral limit, the Poynting flux becomes

$$\mathbf{S} = -\nabla \times \frac{\phi\mathbf{B}}{\mu_0} + \phi\mathbf{j} + \frac{\partial_t\mathbf{A}}{\mu_0} \times \hat{z}, \quad (11)$$

where $\mathbf{j} = \mathbf{\Gamma} - \mathbf{\Gamma}_e$. The last term $\partial_t\mathbf{A} \times \hat{z}/\mu_0$ can also be omitted from the turbulent transport balance as we are interested in quasi steady state energy fluxes, and the total time derivatives vanishes upon time averaging. The term $\phi\mathbf{j}$ seems problematic, as adding a constant to the electrostatic potential would change the Poynting flux. However, its divergence is invariant when adding a constant χ to ϕ ,

$$\nabla \cdot \mathbf{S} = \nabla \cdot (\phi + \chi)\mathbf{j} = \nabla \cdot (\phi\mathbf{j}) + \chi\nabla \cdot \mathbf{j} = \nabla \cdot (\phi\mathbf{j}), \quad (12)$$

since quasineutrality implies $\nabla \cdot \mathbf{j} = 0$.

IV. Ion transport equations

To arrive at the various expressions for the fluxes, we compute the time derivative of the first four moments of the distribution function f using the Vlasov equation (1).

1. Particle density

The zeroth moment of the Vlasov equation yields the continuity equation (5) with the particle flux $\mathbf{\Gamma} = \int \mathbf{v} f d^3v$, written in fluid quantities is $\mathbf{\Gamma} = n\mathbf{u}$ (with the mean velocity \mathbf{u}).

The first moments of the Vlasov equation can be rewritten as

$$\begin{aligned} \partial_t\mathbf{\Gamma} &= \int \mathbf{v} \partial_t f d^3v \\ &= - \int \mathbf{v}\mathbf{v} \cdot \nabla f d^3v - \int \mathbf{v}(-\nabla\phi + \mathbf{v} \times \hat{z}) \cdot \nabla_v f d^3v. \end{aligned} \quad (13)$$

The first integral results in the divergence of the momentum transfer tensor $\nabla \cdot \mathbf{\Pi} = \nabla \cdot \int \mathbf{v}\mathbf{v} f d^3v$, which can be expressed in terms of fluid quantities $\mathbf{\Pi} = \boldsymbol{\pi} + \mathbb{1}p + \mathbf{u}\mathbf{u}n$ (with the stress tensor $\boldsymbol{\pi}$, pressure p and mean velocity \mathbf{u}). The Lorentz force term is modified using integration by parts, resulting in

$$\partial_t\mathbf{\Gamma} = -\nabla \cdot \mathbf{\Pi} - n\nabla\phi + \mathbf{\Gamma} \times \hat{z}. \quad (14)$$

After computing the cross product with the magnetic field \hat{z} , the Grassmann identity can be applied to obtain an expression for the perpendicular particle flux

$$\mathbf{\Gamma}_\perp = -\partial_t\mathbf{\Gamma} \times \hat{z} - \nabla \cdot \mathbf{\Pi} \times \hat{z} - (\nabla\phi \times \hat{z})n. \quad (15)$$

The last term is the $\mathbf{E} \times \mathbf{B}$ particle flux known from gyrokinetics. Since we are interested in quasi steady-state particle fluxes, a time average of the flux is considered, eliminating the time derivative. The other terms vanish when a flux surface average, defined as $\langle \cdot \rangle = \int \cdot, dy, dz / (L_y L_z)$, is applied the expression can be written as

$$\begin{aligned} \langle \nabla \cdot \mathbf{\Pi} \times \hat{z} \rangle + \langle \nabla\phi \times \hat{z}n \rangle &= \hat{x} \langle \langle n\partial_y\phi \rangle \rangle + \partial_x \langle \langle \Pi_{xy} \rangle \rangle \\ &\quad - \hat{y} \langle \langle n\partial_x\phi \rangle \rangle + \partial_x \langle \langle \Pi_{xx} \rangle \rangle. \end{aligned} \quad (16)$$

When the adiabatic assumption (2) is inserted, we obtain

$$\langle \mathbf{\Gamma}_\perp \rangle = -\hat{x}\partial_x \langle \Pi_{xy} \rangle + \hat{y}\partial_x \left(\left\langle \frac{n^2}{2} \right\rangle + \langle \Pi_{xx} \rangle \right). \quad (17)$$

In flux tube scenarios, both terms vanish, as they are total derivatives with respect to x and typically globally averaged quantities are considered.

2. Energy density

The total energy density of the system is given by the sum of the kinetic energy of ions $\epsilon = \int v^2 f / 2 d^3v$ (expressed in thermodynamic quantities $\epsilon = (3/2)p + u^2 n / 2$ with $p = nT$) and the electron energy $\epsilon_e = (n-1)^2 / 2$ derived in section III. The time derivative of the ion kinetic energy is again computed using the Vlasov equation (1)

$$\begin{aligned} \partial_t \epsilon &= \int \frac{v^2}{2} \partial_t f d^3v \\ &= - \int \frac{v^2}{2} \mathbf{v} \cdot \nabla f d^3v \\ &\quad - \int \frac{v^2}{2} (-\nabla\phi + \mathbf{v} \times \hat{\mathbf{z}}) \cdot \nabla_v f d^3v. \end{aligned} \quad (18)$$

Integrating the second integral by parts, yields

$$\partial_t \epsilon = -\nabla \cdot \mathbf{Q} - \int \mathbf{v} \cdot (\nabla\phi) f d^3v, \quad (19)$$

with the total local ion energy flux density $\mathbf{Q} = \int \mathbf{v} v^2 / 2 f d^3v$. Similar to the momentum transfer tensor, the total ion energy flux can be written in terms of the macroscopic fluid quantities $\mathbf{Q} = \mathbf{q} + u^2 n \mathbf{u} / 2 + \mathbf{u} \cdot \boldsymbol{\pi} + (5/2) p \mathbf{u}$, with the heat flux $\mathbf{q} = \int (\mathbf{v} - \mathbf{u})(\mathbf{v} - \mathbf{u}) \cdot (\mathbf{v} - \mathbf{u}) / 2 f d^3v$. The second term in (19) is modified to be expressed as a divergence of the entire integral

$$\partial_t \epsilon = -\nabla \cdot \mathbf{Q} - \nabla \cdot (\phi \boldsymbol{\Gamma}) + \phi \nabla \cdot \boldsymbol{\Gamma}, \quad (20)$$

and inserting (5) results in

$$\partial_t (\epsilon + \phi \partial_t n) = -\nabla \cdot \mathbf{Q} - \nabla \cdot (\phi \boldsymbol{\Gamma}). \quad (21)$$

Utilizing the field equation (2), the electron energy density can be inserted $\partial_t \epsilon_e = \partial_t (n-1)^2 / 2 = \phi \partial_t n$. Apart from the local energy flux density \mathbf{Q} , an additional energy flux $\phi \boldsymbol{\Gamma}$ appears which, can be identified as the sum of the electron energy flux and the Poynting flux $\mathbf{S} + \mathbf{Q}_e = \phi \boldsymbol{\Gamma}$.

The energy flux in the gyrokinetic system is described by the $\mathbf{E} \times \mathbf{B}$ heat flux. This result should be recovered for gyrokinetic modes in the 6D kinetic system. Thus, the kinetic energy flux of the ions should contain the $\mathbf{E} \times \mathbf{B}$ heat flux plus an additional contribution, which cancels $\phi \boldsymbol{\Gamma}$ under the correct conditions.

To establish the connection of the energy flux \mathbf{Q} and the gyrokinetic $\mathbf{E} \times \mathbf{B}$ heat flux, the energy flux can be split into its contributions. For this purpose, the time derivative $\partial_t \mathbf{Q}$ is computed

$$\begin{aligned} \partial_t \mathbf{Q} &= \int \mathbf{v} \frac{v^2}{2} \partial_t f d^3v \\ &= - \int \frac{v^2}{2} \mathbf{v} \mathbf{v} \cdot \nabla f d^3v - \int \frac{v^2}{2} \mathbf{v} (-\nabla\phi + \mathbf{v} \times \hat{\mathbf{z}}) \cdot \nabla_v f d^3v \\ &= -\nabla \cdot \boldsymbol{\Pi}^* - \int \frac{v^2}{2} \mathbf{v} (-\nabla\phi + \mathbf{v} \times \hat{\mathbf{z}}) \cdot \nabla_v f d^3v, \end{aligned} \quad (22)$$

with $\boldsymbol{\Pi}^* = \int v^2 \mathbf{v} \mathbf{v} f / 2 d^3v$. The Lorentz force term is modified using integration by parts and inserting the expression for kinetic energy density ϵ , and the momentum transfer tensor $\boldsymbol{\Pi}$

$$\begin{aligned} &- \int \frac{v^2}{2} \mathbf{v} [(-\nabla\phi + \mathbf{v} \times \hat{\mathbf{z}}) \cdot \nabla_v f] d^3v \\ &= - \int (\nabla\phi \cdot \mathbf{v}) \mathbf{v} f d^3v - \int \frac{v^2}{2} \nabla\phi f d^3v + \int (\mathbf{v} \times \hat{\mathbf{z}}) \frac{v^2}{2} f d^3v \\ &= -\boldsymbol{\Pi} \cdot \nabla\phi - \epsilon \nabla\phi + \mathbf{Q} \times \hat{\mathbf{z}}. \end{aligned} \quad (23)$$

After computing the cross product with the magnetic field $\partial_t \mathbf{Q} \times \hat{\mathbf{z}}$, the Grassmann identity can be applied to obtain an expression for the perpendicular energy flux

$$\begin{aligned} \mathbf{Q}_\perp &= -\partial_t \mathbf{Q} \times \hat{\mathbf{z}} - \nabla \cdot \boldsymbol{\Pi}^* \times \hat{\mathbf{z}} \\ &\quad - \nabla\phi \cdot \boldsymbol{\Pi} \times \hat{\mathbf{z}} - \nabla\phi \times \hat{\mathbf{z}} \epsilon. \end{aligned} \quad (24)$$

Computing the time and flux surface average of this equation yields

$$\langle \mathbf{Q}_\perp \rangle = -\langle \nabla\phi \times \hat{\mathbf{z}} \epsilon \rangle - \langle \nabla\phi \cdot \boldsymbol{\Pi} \times \hat{\mathbf{z}} \rangle - \langle \nabla \cdot \boldsymbol{\Pi}^* \times \hat{\mathbf{z}} \rangle. \quad (25)$$

Next to the $\mathbf{E} \times \mathbf{B}$ heat flux $\mathbf{Q}^{E \times B} = \nabla\phi \times \hat{\mathbf{z}} \epsilon$, two more contributions can be identified. In order to compare their relevance for the total energy balance (21), we also express the Poynting flux in terms of the contributions from equation (15)

$$\mathbf{S}_\perp = \phi \boldsymbol{\Gamma}_\perp = -\phi \partial_t \boldsymbol{\Gamma} \times \hat{\mathbf{z}} - \phi \nabla \cdot \boldsymbol{\Pi} \times \hat{\mathbf{z}} - \phi (\nabla\phi \times \hat{\mathbf{z}}) n. \quad (26)$$

To study quasi steady-state energy flux, the quantities are time-averaged, effectively removing the time derivative of the energy flux, $\partial_t \mathbf{Q}$. In contrast, the time average of $\phi \partial_t \boldsymbol{\Gamma}$ does not vanish. In summary, the flux surface average of the total energy balance from equation (21) is given by

$$\begin{aligned} \partial_t \langle \epsilon + \phi \partial_t n \rangle &= -\hat{\mathbf{x}} \partial_x \cdot \langle \mathbf{Q} + \phi \boldsymbol{\Gamma} \rangle \\ &= -\hat{\mathbf{x}} \partial_x \cdot \langle -\nabla\phi \times \hat{\mathbf{z}} \epsilon - \nabla\phi \cdot \boldsymbol{\Pi} \times \hat{\mathbf{z}} - \nabla \cdot \boldsymbol{\Pi}^* \times \hat{\mathbf{z}} \\ &\quad - \phi n \nabla\phi \times \hat{\mathbf{z}} - \phi \nabla \cdot \boldsymbol{\Pi} \times \hat{\mathbf{z}} - \phi \partial_t \boldsymbol{\Gamma} \times \hat{\mathbf{z}} \rangle \end{aligned} \quad (27)$$

The two terms containing the momentum flux tensor $\boldsymbol{\Pi}$ can be combined

$$\langle (\boldsymbol{\Pi} \cdot \nabla\phi) \times \hat{\mathbf{z}} \rangle + \langle (\phi \nabla \cdot \boldsymbol{\Pi}) \times \hat{\mathbf{z}} \rangle = \langle \nabla \cdot (\phi \boldsymbol{\Pi}) \rangle \times \hat{\mathbf{z}} \quad (28)$$

resulting in total energy balance

$$\begin{aligned} \partial_t \langle \epsilon + \phi \partial_t n \rangle &= -\hat{\mathbf{x}} \partial_x \cdot \langle -\epsilon \nabla\phi - \nabla \cdot (\phi \boldsymbol{\Pi} + \boldsymbol{\Pi}^*) - \phi \partial_t \boldsymbol{\Gamma} - \phi n \nabla\phi \rangle \times \hat{\mathbf{z}}. \end{aligned} \quad (29)$$

The last term $\langle \phi n (\nabla\phi \times \hat{\mathbf{z}}) \rangle$ is the Poynting flux caused by the $\mathbf{E} \times \mathbf{B}$ particle flux which averages away in the flux surface average for adiabatic electrons

$$\langle \phi (\nabla\phi \times \hat{\mathbf{z}}) n \rangle = \langle n^2 \nabla\phi \rangle \times \hat{\mathbf{z}} = \nabla \langle \frac{n^3}{3} \rangle \times \hat{\mathbf{z}} = 0, \quad (30)$$

when the field equation (2) is inserted, because odd powers of a perturbed quantity average out. Similarly to the particle flux

induced by the momentum transfer tensor, $\langle \nabla \cdot (\phi \mathbf{\Pi} + \mathbf{\Pi}^*) \rangle \times \hat{z}$ can be further simplified,

$$\partial_x \hat{x} \cdot \langle \nabla \cdot (\phi \mathbf{\Pi} + \mathbf{\Pi}^*) \rangle \times \hat{z} = \partial_x^2 \langle \phi \Pi_{xy} + \Pi_{xy}^* \rangle. \quad (31)$$

Inserting these two simplification into (29) results in the energy balance for kinetic ions with adiabatic electrons

$$\partial_t \langle \epsilon + \epsilon_e \rangle = -\partial_x \langle -\epsilon \partial_y \phi - \partial_x (\phi \Pi_{xy} + \Pi_{xy}^*) - \phi \partial_t \Gamma_y \rangle. \quad (32)$$

In summary, the total energy flux in the fully kinetic systems contains two contributions beyond the well-known gyrokinetic heat flux.

Firstly, the additional energy flux induced by $\mathbf{\Pi}$ and $\mathbf{\Pi}^*$. This term arises from the radial dependency of the background profiles. In global gyrokinetic simulations, a similar energy flux would occur, driven by the $\mathbf{\Pi}$ and $\mathbf{\Pi}^*$ tensors resulting from the gyrotransformation from gyrocenter to particle coordinates.

For $k_x = 0$, this term vanishes, leaving only the kinetic energy flux associated with the $\mathbf{E} \times \mathbf{B}$ heat flux. The remaining difference compared to gyrokinetics is the Poynting flux component $\phi \partial_t \mathbf{\Gamma}$. This can be neglected for gyrokinetic modes with $\omega \ll 1$, but it might become relevant for high-frequency modes with $\omega \gtrsim 1$, such as IBW turbulence [6].

V. Simulation of energy fluxes

1. Energy flux for gradients in Boussinesq approximation

For the first numerical test, we investigate the ion temperature gradients (ITG) instability previously shown in [7]. For the simulation, we introduce a temperature gradient source term on the RHS

$$\partial_t \delta f + \mathbf{v} \cdot \nabla \delta f + [-\nabla \phi + (\mathbf{v} \times \hat{z})] \cdot \nabla_v \delta f = \nabla \phi \cdot \nabla_v g_0, \quad (33)$$

where g_0 is the background distribution function

$$g_0(\mathbf{R}, v_\perp, v_z) = \left(\frac{n(\mathbf{R})}{2\pi T(\mathbf{R})} \right)^{\frac{3}{2}} \exp\left(-\frac{[v_\perp^2 + v_z^2]}{2T(\mathbf{R})}\right) \quad (34)$$

and \mathbf{R} is the gyrocenter coordinates $\mathbf{R} = \mathbf{r} - \boldsymbol{\rho}$ (where $\boldsymbol{\rho}$ is the Larmor radius vector). The gradient on the right-hand side is given by (for clarification, we introduce a notation to specify which variable is held constant for the partial derivative, i.e. $(\nabla_v f)_\mathbf{r}$ for a derivative with respect to \mathbf{v} at fixed \mathbf{r})

$$\begin{aligned} (\nabla_v g_0)_\mathbf{r} &= \hat{z} \times (\nabla_{\mathbf{R}} g_0)_\mathbf{v} + (\nabla_v g_0)_\mathbf{R} =: \mathbf{v}^* g_0 + (\nabla_v g_0)_\mathbf{R} \\ &= -g_0 \hat{z} \times \left(\frac{\nabla T}{T} \frac{3 - (v_\perp^2 + v_z^2)}{2} \right) + (\nabla_v g_0)_\mathbf{R}. \end{aligned} \quad (35)$$

The limit that the gradient length is infinite $T(\mathbf{R}) \rightarrow T = 1$ is taken, such that the background distribution is independent of \mathbf{R} . Thus, g_0 is replaced with the homogeneous Maxwellian distribution $f_M = \exp(-v^2/2)/(2\pi^{3/2})$.

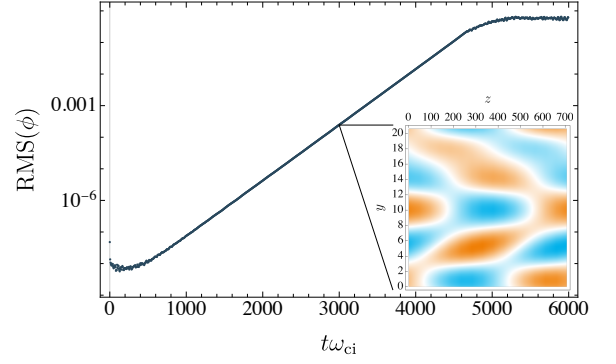


FIG. 1: Time evolution of electrostatic potential amplitude with snapshot of perturbation in $y-z$ plane

To numerically measure the transport values, we have conducted a 2D3V simulation of an ITG instability. The box has been chosen with dimensions $L_y = 20/3\pi$, $L_z = 240\pi$ and $(N_y, N_z) = (64, 16)$. It has been shown in previous works that due to the small wave numbers in parallel direction, the small number of points in z -direction is sufficient [8]. For the given box dimensions, the smallest perpendicular wave number is $k_{y,0} = 0.3$. The length in the parallel direction is determined by the wave number of the fastest-growing mode in the system, which depends on the temperature gradient. Employing a temperature gradient of $\partial_x \log T = 0.1$, we obtained an ideal parallel wave number of $k_z = 1/120$.

Velocity space is symmetric in all directions, with $v_{\max} = 4$ (or $v_{\max} = 6$) and $(N_{v_x}, N_{v_y}, N_{v_z}) = (33, 33, 33)$. We applied periodic boundary conditions across all six dimensions. The interpolation utilizes a 7th-order Lagrange stencil for the velocity directions and an 8th order stencil for the spatial directions. From the simulation, we can extract the necessary moments of the distribution function and compute the relevant energy fluxes for our comparison. Figure 1 shows the root-mean-square (RMS) of the electrostatic potential as a function of time. We see a linear growth for the time between $t \sim 1000 - 4500$ and nonlinear saturation at around $t \sim 5000$. As an inset we show a snapshot at $t = 3000$ of the electrostatic potential in the $y-z$ plane, showing the clear ITG mode structure, of the dominate mode with $\mathbf{k} = (0, 3/5, 1/120)$.

It has been discussed in section IV that the flux surface averaged particle flux is zero. This should be investigated first. For this purpose we have calculated the particle flux $\langle \Gamma_x \rangle = \langle \int v_x f d^3v \rangle$ and the $\mathbf{E} \times \mathbf{B}$ particle flux $\langle \Gamma_x^{\mathbf{E} \times \mathbf{B}} \rangle = \langle \nabla \phi \times \hat{z} n \rangle$. Figure 2 shows both quantities normalized to the square of the fluctuation amplitude of the electrostatic potential for two separate simulations with different maximal velocities.

The results show that the particle flux is zero up to numerical errors, which are constant (ratio with fluctuation amplitude decreases with growing electrostatic potential). An error proportional to the square of the electrostatic potential occurs at the later stage of the simulation. By increasing the size of the velocity grid from $v_{\max} = 4$ to $v_{\max} = 6$, this error can be reduced by 4 orders of magnitude, suggesting that the error

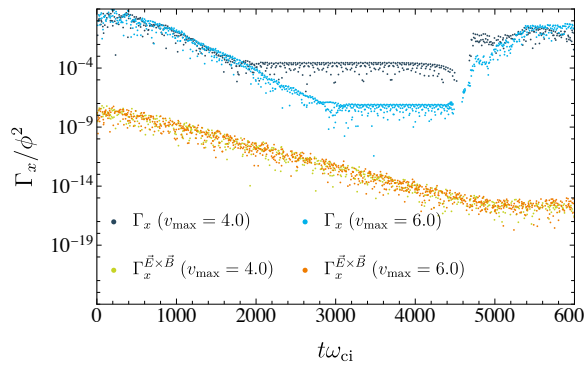


FIG. 2: Comparison of flux surface averaged particle flux with $\mathbf{E} \times \mathbf{B}$ particle flux for simulation with $v_{\max} = 4$ and $v_{\max} = 6$. All quantities are normalized to the square amplitude of the electrostatic potential

origins from the boundaries in velocity space.

In previous work, we have analytically calculated the $\mathbf{E} \times \mathbf{B}$ energy flux and the Poynting flux [7]. Here, we investigate the equivalence presented in equation (24). The top plot in figure 3 illustrates the contributions from the $\mathbf{E} \times \mathbf{B}$ = heat flux $Q^{\mathbf{E} \times \mathbf{B}} = \epsilon \nabla \phi \times \hat{z}$, the stress-induced energy flux $Q^{\Pi} = \nabla \cdot \Pi \times \hat{z}$, and $Q = \int v v^2 f / 2d^3 v$. The middle and lower plots compare the LHS and RHS of equation (25) and show the error for different v_{\max} values. All quantities are normalized to the square of the perturbation amplitude of the electrostatic potential. The results highlight one of the main advantages of the presented method for calculating energy fluxes. The directly computed energy flux $Q = \int v v^2 f / 2d^3 v$ exhibits significantly more oscillations than the computed $\mathbf{E} \times \mathbf{B}$ heat flux and the stress-induced energy flux. These strong oscillations in the total flux account for the majority of the error during the early initialization and the nonlinear stage of the simulation. In the linear phase, however, the two calculation methods show very good agreement. As for the particle flux, we observe an error arising from the boundary in velocity space, which is proportional to the square of the wave amplitude.

2. Nonlinear gradients

This section shifts away from the Boussinesq gradients described in the previous section towards a nonlinear treatment of gradients in our simulation code. The initial condition in the simulation is chosen such that the distribution function contains density and temperature profiles as written in (34). The background profiles $n(\mathbf{R})$ and $T(\mathbf{R})$ are defined in gyrocenter coordinates $\mathbf{R} = \mathbf{r} - \boldsymbol{\rho}$ to remove oscillations with the Larmor frequency. To simplify the treatment of boundary conditions, the profiles are periodic using sine-profiles in the x -direction

$$n(x, v_y) = 1 + \kappa_n \sin(k_0(x - v_y)), \quad (36)$$

$$T(x, v_y) = 1 + \kappa_T \sin(k_0(x - v_y)). \quad (37)$$

The initial background density gradient should not induce an electric field. Therefore, modes with wave numbers parallel to

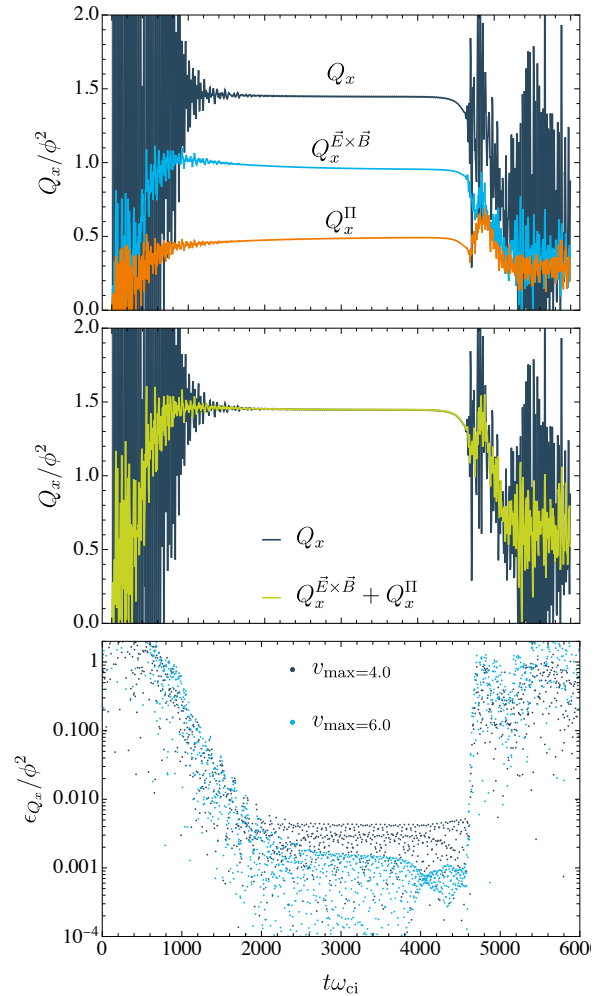


FIG. 3: Comparison of the energy flux $Q = \int v^2 f / 2d^3 v$ with its contributions derived in equation (24) (top, middle) and error for simulation with $v_{\max} = 4$ and $v_{\max} = 6$ (bottom). All quantities are normalized to the square amplitude of the electrostatic potential

the gradient are eliminated from the electrostatic potential by subtracting the flux surface average

$$\phi = n - \langle n_0 \rangle, \quad (38)$$

where n_0 is the density perturbation at $t = 0$. When selecting parameters for the background profile, it is crucial to ensure that the wavelength of the unstable mode, $\lambda_{\text{ITG}} = 2\pi/k_y$, is shorter than the typical gradient length of the profile, $1/L_T \sim \partial_x \ln T(x)$.

For our initial simulation, we chose parameters: $\kappa_n = 0$, $\kappa_T = 0.5$, and $k_0 = 0.2$, resulting in a temperature gradient $\max_{x \in [0, L_x]} \partial_x \log T(x) = 0.115$, where L_x denotes the box length in the x -direction. The simulation has been conducted on a box with a length of $L = 10\pi \times 2.5\pi \times 240\pi$, $N = 128 \times 32 \times 16 \times 32 \times 32 \times 16$ and $\delta t = 0.02$.

The top plot in figure 4 shows an x - y -cross-section of the electrostatic potential just before the non-linear saturation, highlighting two modes growing on the two slopes of the temper-

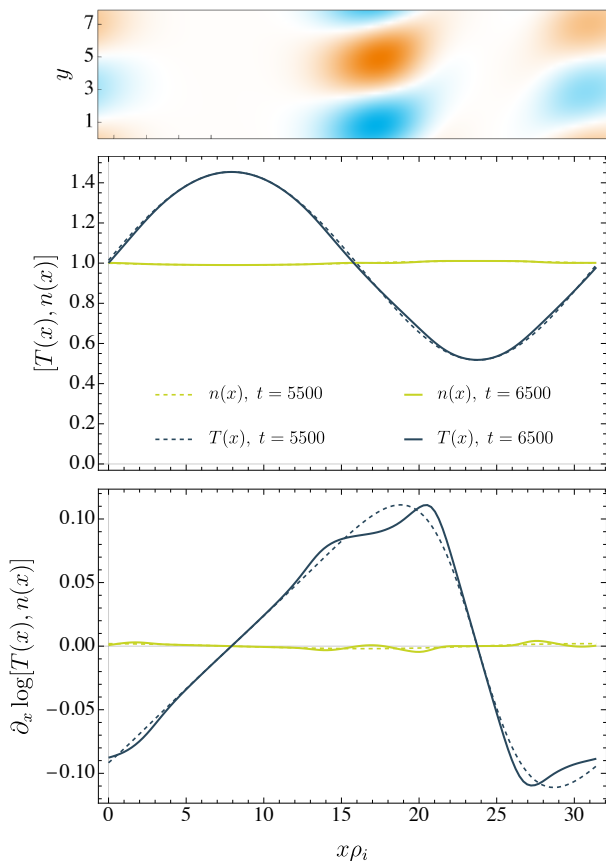


FIG. 4: Cross section of electrostatic potential perturbation in $x - y$ -plane in linear phase ($t = 6000$) (top). Profiles (middle) and logarithmic gradient (bottom) of particle density and energy density for two different times

ature profile. The second plot shows density and temperature profiles at two different times, indicating a slight decay. The decay is more evident when plotting the logarithmic gradients of the profiles (Figure 4, bottom), where the erosion of the gradients by the mode is visible.

The change of the local energy density can be compared to the divergence to the energy fluxes computed from the different methods discussed in section IV. Figure 5 shows a comparison between the change of the total energy $\partial_t \langle \epsilon + \epsilon_e \rangle$ with the divergence total energy transport $\nabla \cdot (\mathbf{Q} + \mathbf{Q}_e + \mathbf{S})$ directly computed from the distribution function and the expression derived in equation (29) for $t = 6000$. At this point, the nonlinear saturation has begun, but the turbulence has not fully developed yet (see figures 4). The plot shows a very good agreement between the two different approaches for computing the energy flux, showing that the decomposition of the energy fluxes in its contributions in equation (29) is correct. Comparing the divergence of the energy flux to the change in local energy density, we find that the local change rate of the total energy is lower by approximately 10 – 15%. The modes are confined to a relatively narrow radial area. The high wavenumber k_x amplifies the effect of the radial dependency of the heat flux, which could lead to a discrepancy. Furthermore, the strong

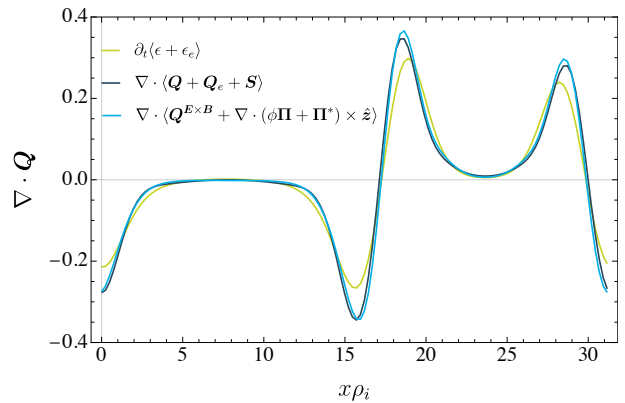


FIG. 5: Comparison between change of energy density $\partial_t \langle E \rangle$ and divergence of energy fluxes $\nabla \cdot \mathbf{Q}$ at $t = 6000$

radial dependency of the heat flux can introduce numerical errors, owing to the limited accuracy of Lagrange interpolation at high wavenumbers. The time derivative of the changing total energy is computed using a finite difference derivative averaged over exactly one Larmor period to remove the contributions from the $\partial_t \mathbf{Q} \times \hat{\mathbf{z}}$ term in equation (24). Increasing numerical resolution is currently not feasible due to the high computational cost.

VI. Summary

In this work, we have introduced a novel method for calculating energy flux in the 6D kinetic description of ions in a plasma. The method rewrites the energy flux (kinetic energy flux and Poynting flux) in terms of other moments of the distribution function. Figure 3 shows that this approach reduces oscillations in the diagnostic, leading to more reliable results. Additionally, it enables us to identify various contributions to the energy balance and attribute physical interpretations to individual components. This has helped to recognize the connection to the $\mathbf{E} \times \mathbf{B}$ heat flux known from gyrokinetics and the contributions from the radial dependency of background profiles. Moreover, it has enabled us to identify a potential candidate for a difference in the energy flux for non-gyrokinetic high-frequency modes. The effect of the $\phi \partial_t \mathbf{\Gamma}$ contribution, which has been neglected due to the low frequency of ITG modes, requires further investigation for waves with $\omega \gtrsim 1$. The proposed framework could be extended to rewrite higher moments of the distribution function, such as the momentum transfer tensor $\mathbf{\Pi}$ and the $\mathbf{\Pi}^*$ tensor, using the same method. However, this would introduce a dependency of the energy balance on higher-rank tensors, making the framework less practical, and it would complicate the interpretation of the additional terms. The conditions under which this continued expansion would converge remain an open question.

Acknowledgments

This work has been carried out partly within the framework of the EUROfusion Consortium, funded by the European Union via the Euratom Research and Training Programme (Grant Agreement No 101052200 – EUROfusion). Support has also been received by the EUROfusion High Performance Computer (Marconi-Fusion). Views and opinions expressed

are however those of the author(s) only and do not necessarily reflect those of the European Union or the European Commission. Neither the European Union nor the European Commission can be held responsible for them. Numerical simulations were performed at the MARCONI-Fusion supercomputer at CINECA, Italy and at the HPC system at the Max Planck Computing and Data Facility (MPCDF), Germany.

-
- [1] J. Candy, E. Belli, and R. Bravenec. A high-accuracy eulerian gyrokinetic solver for collisional plasmas. *Journal of Computational Physics*, 324:73–93.
 - [2] K. Hallatschek. Thermodynamic potential in local turbulence simulations. *Physical Review Letters*, 93(12):125001.
 - [3] F. Jenko. Massively parallel vlasov simulation of electromagnetic drift-wave turbulence. *Computer Physics Communications*, 125(1):196–209.
 - [4] E. Lanti, N. Ohana, N. Tronko, T. Hayward-Schneider, A. Bottino, B. McMillan, A. Mishchenko, A. Scheinberg, A. Biancalani, P. Angelino, S. Brunner, J. Dominski, P. Donnel, C. Gheller, R. Hatzky, A. Jocksch, S. Joliet, Z. Lu, J. Martin Collar, I. Novikau, E. Sonnendrücker, T. Vernay, and L. Villard. Orb5: A global electromagnetic gyrokinetic code using the PIC approach in toroidal geometry. *Computer Physics Communications*, 251:107072.
 - [5] N. Noreen, F. Riaz, S. Malik, and S. Zaheer. Ion Bernstein mode instability with ring velocity distribution function. *Progress of Theoretical and Experimental Physics*, 2019(5):053E01.
 - [6] M. Raeth and K. Hallatschek. High-frequency nongyrokinetic turbulence at tokamak edge parameters. *Physical Review Letters*, 133:195101, Nov 2024.
 - [7] M. Raeth, K. Hallatschek, and K. Kormann. Simulation of ion temperature gradient driven modes with 6d kinetic vlasov code. *Physics of Plasmas*, 31(4):042101.
 - [8] M. R ath. Beyond gyrokinetic theory: Excitation of high-frequency turbulence in 6d vlasov simulations of magnetized plasmas with steep temperature and density gradients.
 - [9] N. Schild, M. Raeth, S. Eibl, K. Hallatschek, and K. Kormann. A performance portable implementation of the semi-lagrangian algorithm in six dimensions. *Computer Physics Communications*, 295:108973.
 - [10] N. Schild, M. Raeth, K. Hallatschek, and K. Kormann. Convergence of splitting methods on rotating grids for the magnetized vlasov equation.
 - [11] P. H. Yoon, F. Hadi, and A. Qamar. Bernstein instability driven by thermal ring distribution. *Physics of Plasmas*, 21(7):074502.